

This AAM is provided for your own personal use only. It may not be used for resale, reprinting, systematic distribution, emailing, or for any other commercial purpose without the permission of the publisher.

The following publication Zeng, G.-Z., Li, Z.-W., Huang, S. and Chen, Z.-W. (2023), "Influence of wind and rain environment on operational safety of intercity train running on the viaduct", *International Journal of Numerical Methods for Heat & Fluid Flow*, Vol. 33 No. 4, pp. 1584-1608 is published by Emerald and is available at <https://doi.org/10.1108/HFF-12-2022-0693>.

# Influence of Wind and Rain Environment on Operational Safety of Intercity Train Running on the Viaduct

## Abstract

**Purpose** – Based on the aerodynamic loads and dynamic performances of trains, this article investigates the effect of crosswinds and raindrops on intercity trains operating on viaducts to ensure the safe operation of intercity railways in metropolitan areas.

**Design/methodology/approach** – An approach coupled with the Euler multiphase model as well as the standard  $k-\varepsilon$  turbulence model is utilized to investigate the coupled flow feature surrounding trains and viaducts, including airflow and raindrops, and the numerical results are validated with those of the wind tunnel test. Additionally, the train's dynamic response and the operating safety region in different crosswind speeds and rainfall is investigated based on train's aerodynamic loads and the train wheel-rail dynamics simulation.

**Findings**—The aerodynamic loads of trains at varying running speeds exhibit an increasing trend as the increase of wind speed and rainfall intensity. The motion of raindrop particles demonstrates a significant similarity with the airflow in wind and rain environments, as a result of the dominance of airflow and the supplementary impacts of droplets. As the train's operating speed ranged between 120–200 km/h and within a rainfall range of 20–100 mm/h, the safe operating region of trains decreased by 0.56% to 7.03%, compared with the no-rain condition (0 mm/h).

**Originality/value**—The impact of crosswind speeds and rainfall on the train's aerodynamic safety is studied, including the flow feature of crosswind and different particle-sized raindrops around the train and viaduct, aerodynamic loads coefficients suffered by the intercity train as well as the operating safety region of intercity trains on the viaduct.

**Keywords** crosswind and raindrops; aerodynamic performance; intercity train; operational safety

**Paper type** Research paper

## 1. Introduction

In recent years, people communication and freight transportation demonstrate a more frequent tendency between the regions of urban agglomerations, owing to the growth of the economy and the gradual formation of metropolitan areas as well as city clusters (Pietrzak and Pietrzak, 2021). As an essential subsystem of city clusters, intercity rail transits play an increasingly vital role in meeting the growing demand for speedy commuting for people living in urban agglomerations, with its characteristics of high speed, large volume and environmental protection (Yu *et al.*, 2018; Zeng *et al.*, 2019; Xu *et al.*, 2022). Establishing an intercity railway system that matches the development of regional cities becomes an indispensable part of modern urban agglomerations and an important part of promoting regional economic development (Zhang *et al.*, 2020).

While increasing the running speed of trains brings convenience to intercity commuting, a series of operational safety problems will also become more prominent (Yang *et al.*, 2019; Zhou *et al.*, 2020; Chen *et al.*, 2022b; Liu *et al.*, 2022; Niu *et al.*, 2022). In a complex crosswind environment, such as an embankment or viaduct, the train's aerodynamic performance and index of operational safety will change dramatically (Diedrichs *et al.*, 2007; Li *et al.*, 2011a; Giappino *et al.*, 2016; Baker and Sterling, 2018; Zhang *et al.*, 2018; Li *et al.*, 2022a; Yang *et al.*, 2022), which seriously threatens the stability, safety and ride comfort of the train's operation (Avila-Sanchez *et al.*, 2017; Chen *et al.*, 2018; Chen *et al.*, 2019a; Jin *et al.*, 2020; Chen *et al.*, 2021). In addition, the flow field surrounding the train varies dramatically as it over viaducts, because of the frequent occurrence of convective weather, such as the strong wind with rain, in the metropolitan agglomeration along the southeast coast of China (Chen *et al.*, 2016). Fall-off raindrops driven by crosswinds impact the surface of the running trains and collide and splash on it, which makes raindrops cover and alter the roughness and unevenness of the train surface, affecting the aerodynamic loads suffered by the train (Yu *et al.*, 2021). Caused by multifactor, safety problems of trains running on the viaduct in strong crosswind and rain conditions are particularly prominent. As a result, ensuring the safe operation of intercity trains running over viaducts in severe weather has become a crucial issue.

Domestic and abroad researchers, in the past, analyzed and evaluated the stability and safety of trains under crosswind environments based on the theory of vehicle dynamics, while the adopted methods can be divided into the full-scale test, bench test and numerical simulation. Since the 1960s, Japan (Ikemori, 1978), China (Bian *et al.*, 2014), and other counties have measured the stability of trains based on the full-scale test and bench test, which provides an essential reference to the relevant research through this experiments (Jiang *et al.*, 2022; Zou *et al.*, 2022). Nevertheless, the full-scale test also shows its limitations in practice, such as the long test period, low repeatability and difficulty obtaining test results under extreme conditions. Thus, a combinational method based on computational fluid dynamics and multi-body dynamic simulation was proposed and utilized to analyze and evaluate the operational stability of trains running on the viaduct (Li *et al.*, 2013; Tao *et al.*, 2022; Wen *et al.*, 2022). For instance, Mao *et al.* (2011) analyzed parameters of the dynamic performance of trains in different crosswind speeds and train speeds, and critical speeds of the safe running of trains are obtained based on the evaluation standard of high-speed train running stability. Zhang *et al.* (2013) established the multi-body dynamic model of the train and bridge to investigate the influence of wind barriers on the bridge dynamic response and train dynamic performance under crosswind actions. Based on the wheel-rail contact friction theory, Olmos and Astiz (2018) utilized the train-bridge-wind field model to analyze the crosswind effect on trains running on the viaduct and the tolerated wind speed of trains crossing the bridge. To ensure the train safely operates on the Volga River Bridge from Moscow to Kazan in Russia, Montenegro *et al.* (2020) compared the dynamic responses with two types of train-bridge combined systems to conclude the critical crosswind speed under the different running speeds of trains.

With the advancement of computing technology, to more realistically study the impact of weather factors on the aerodynamic effect of structures, the influence of wind-driven raindrops on buildings, bridges and

transportation have gotten widespread attention in recent years (Coelho and Henriques, 2016; Chen *et al.*, 2022a). However, constrained by technical conditions, it is challenging to examine the aerodynamic performance of trains in wind and rain environments through experiments. Therefore, research on trains running on the ground under this severe scenario was conducted mostly based on numerical models. For instance, by using the Euler multiphase model, Shao *et al.* (2011) analyzed how the aerodynamic forces exerted on a train changed as the crosswind speed and rainfall changed. Li *et al.* (2020) investigated pressure coefficient and velocity coefficient distribution around the train under the different trains' speeds and rainfall amounts using the Eulerian-Lagrangian approach. Based on the discrete phase model, aerodynamic load coefficients for trains running on the ground in wind and rain were discovered to correlate with rainfall intensity at different operating speeds by Yu *et al.* (2022).

Based on the aforementioned studies, the operational safety of high-speed trains under the complicated wind environment has achieved advancement, especially for ground-running trains. Nevertheless, the relevant research on train safety when it operates on the viaducts in coupled crosswind and raindrops environments is still in its infancy, and it is quite different from trains running on the ground that solely suffer crosswind force. In this work, an approach based on the Euler multiphase model is utilized to analyze the coupled flow feature surrounding the train and viaduct, including airflow and raindrops. Additionally, the safe operating region for trains on the viaduct is concluded, according to train's dynamic response under the combined impact of wind and rain.

The research method and numerical model are described in Section 2 of this work. Section 3 provides the results of the analysis and discussions. Section 4 concludes by summarizing the main findings and suggesting themes for future research.

## 2. Numerical method

### 2.1 Geometry model

Figure 1 shows the intercity train model addressed in this work. It comprises three vehicles in total: a head car, a middle car, and a tail car, with entire lengths of 76.3 m. The width and height of the train is 3.3 m and 4.2 m, respectively. Furthermore, the viaduct's entire width and height are 12.2 m and 3.5 m, respectively, while the height of the viaduct deck from the ground is 15.0 m.

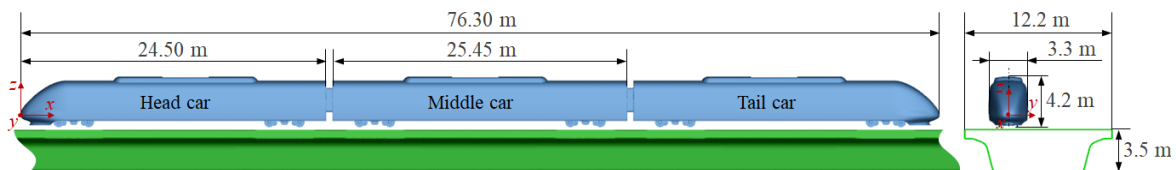


**Figure 1.** Intercity train and viaduct model

## 2.2 Wind and rain environment parameters

### 2.2.1 Wind field initial conditions

The lower atmospheric boundary layer wind fields were used as an initial condition for simulating the wind and rain environment to accurately investigate the influence of crosswinds and raindrops on flow fields surrounding the train and viaduct. Based on this, the wind profile based on horizontal homogeneous terrain, which has been widely employed in previous studies (Xi *et al.*, 2012), is adopted. The expression of the wind profile can be written as follow:

$$V_w / V_r = (h / h_0)^\alpha \quad (1)$$

where,  $V_w$  is given by the monitoring wind speed at different altitudes, and the mean monitoring wind speed at the reference altitude is represented by  $V_r$ .  $h$  and  $h_0$  contribute to the altitudes of the measuring point and reference altitudes, respectively, and  $\alpha$  is the roughness index of the ground. According to railway terrains investigations in the past (Lai *et al.*, 2006; Zhang *et al.*, 2006; Lu *et al.*, 2012; Liu *et al.*, 2018),  $h_0 = 10$  m and  $\alpha = 0.16$  m in the open terrain are adopted herein. In the current work, the crosswind speeds between 10 and 30 m/s and with 5 m/s intervals are taken into consideration.

### 2.2.2 Parameters of rainfall environment

The rainfall intensity is defined in meteorological terms as the average volume of rainfall over a period of time and is often described as hourly rainfall. Based on this, five categories can be graded as light rain, moderate rain, heavy rain, torrential rain and downpour. Due to the strong randomness of the rainfall process, the distribution of raindrops can show complex and diverse variations in different regions and at different times. To investigate the coupled effect of environmental wind and raindrops, the raindrop spectrum is adopted in this paper to split all raindrops into distinct groups, which is defined by the modified  $\Lambda$  distribution function (de Wolf, 2001).

$$N(D, R) = N_0 D^\beta e^{-\Lambda D} \quad (2)$$

where,  $D$  donates the diameters of raindrops;  $\beta$  is an exponential constant and is equal to 2.93;  $N_0$  and  $\Lambda$  are the functions correlated to the rainfall intensity  $R$ , which can be expressed as follows, under standard atmospheric pressure:

$$N_0(R) = 1.98 \times 10^{-5} R^{0.186} \left[ 1.047 - 0.0436 \ln(R) + 0.00734 (\ln(R))^2 \right] \quad (3)$$

$$\Lambda(R) = 5.38 \times R^{0.186} \quad (4)$$

Raindrops' velocity rises with increasing falling distance until the effect of aerodynamic drag and gravity attain equilibrium and drop uniformly. The Atlas model is adopted, which is a simplification of real observed data and allows for the representation of raindrops' terminal velocity (Huang and Li, 2010), and the variation

of the terminal velocity of different diameters of raindrops are shown in Figure 2.

$$V_r(D) = \begin{cases} 0; & D \leq 0.03 \text{ mm} \\ 4.323(D-0.03); & 0.03 \text{ mm} < D \leq 0.6 \text{ mm} \\ 9.65 - 10.3e^{-0.6D}; & D > 0.6 \text{ mm} \end{cases} \quad (5)$$

In addition, the volume fraction is an important parameter to indicate different rainfalls in simulating the rainfall scenario. Each rain phase's volume fraction  $a_k$  with different diameters of raindrops, therefore, can be defined, given by the determined terminal velocity, rainfalls and raindrop size distribution (Wang *et al.*, 2019):

$$a_k = \frac{Rf_h(D, R) 1 \times 10^{-3}}{V_t(D)} \quad (6)$$

where,  $f_h(D, R)$  is defined as the rain flux fraction that relates to raindrops diameters, as expressed below (Wang *et al.*, 2019):

$$f_h(D, R) = \frac{D^3 N(D, R) V_t(D)}{\int_0^{\infty} D^3 N(D, R) V_t(D) dD} \quad (7)$$

In this work, the raindrop size in a range of 0.25-1.50 mm is chosen for simulating the rainfall scenario, due to the raindrop particles in this range showing an extremely high degree of concentration in their volume fraction at different rainfalls, as shown in Figure 3. As in the aforementioned formulas, raindrop distribution is represented by the collection of particles of equal size, so raindrop practices are grouped with an interval of 0.25 mm. For the analysis, rainfall from 0 to 100 mm/h (with a 20 mm/h interval) is taken into consideration to represent the most common rainfall scenario in urban areas.

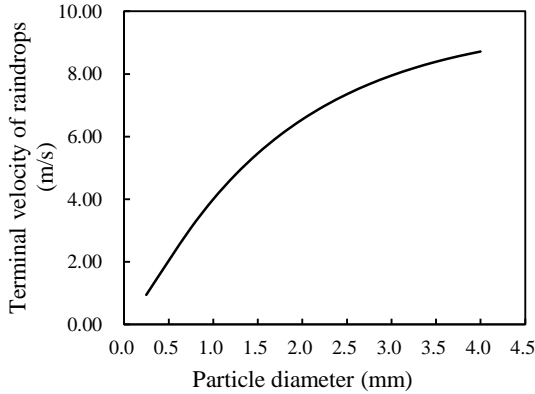


**Figure 2.** The terminal velocity of different diameter raindrops.

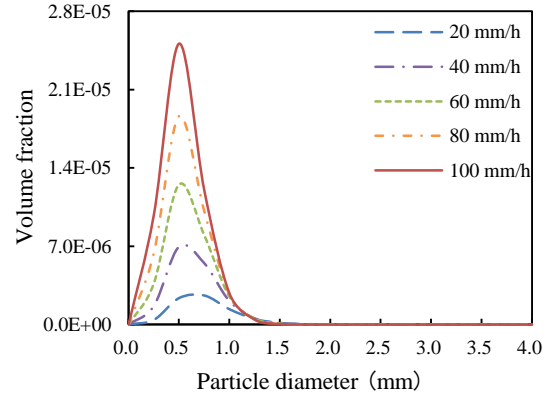


**Figure 3.** Volume fraction of different diameters of raindrops for varied rainfall.

### 2.3 Computational domain and boundary condition

For simulating the wind and rain environment accurately and effectively, it is necessary to consider the full development of the flow field and maintain sufficient space for the interaction between the incoming initial airflows as well as raindrops during the establishment of the computational domain. The computing domain, therefore, with dimensions of  $53H \times 72H \times 20H$  is used for numerical simulation in this work, where  $H$

denotes the train's height, as shown in Figure 4. The distance from the face ABCD to the nose point of the head car is  $24H$ , and the identical distance is set from the nose point of the head car to the face BFGC.

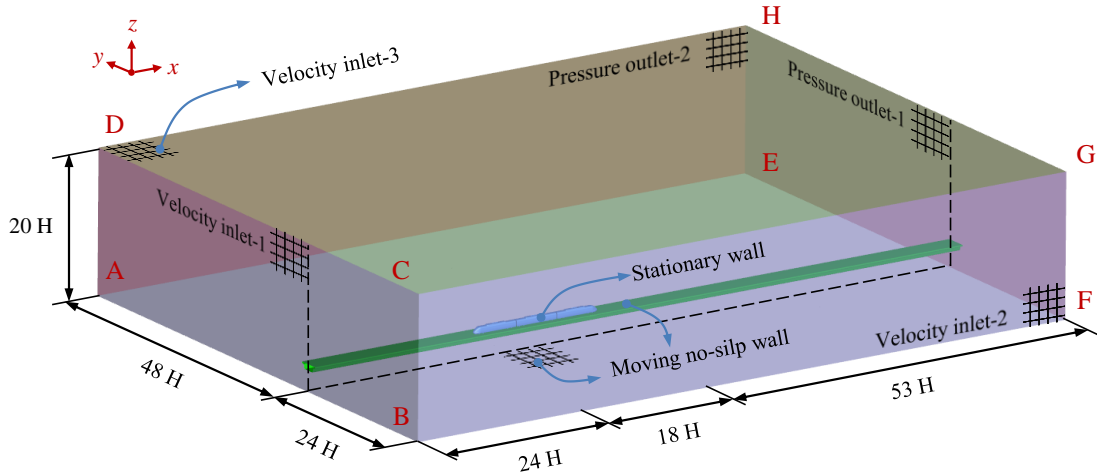


**Figure 4.** Computational domain

The faces ABCD and BFGC are set as the velocity-inlet boundary condition. The velocity component is invoked in the velocity-inlet boundary conditions to initiate the synthetic coming flow, as shown in Figure 5. The zero pressure-outlet boundary condition is implemented at the faces EFGH and AEHD. In addition, zero input values are used for the DCGH boundary conditions at the velocity inlets at the top surface to guarantee that the numerical results may be compared with the conditions with raindrops. With respect to the flow field surrounding the structures, the crosswind-only scenario would not be affected by the top surface boundary condition since it is far away from the placed geometry. The stationary wall boundary condition is used on the train surface. The moving no-slip wall conditions are adopted on the viaduct surface and ground, setting the velocity component along the flow direction equal to the running speed of the train, to simulate the flow impact of train movement over the viaduct and ground accurately.

Because the impact of the rain phase should be addressed while modeling the wind and rain environment, the parameters of rainfall are inputted as an initial value into the boundary conditions. Considering the driving effect of crosswinds on raindrops, the droplets are set to release from the boundary face of DCGH, ABCD, and BFGC. In addition, due to the raindrop particles are highly susceptible to the driving effect of the crosswind (Wang *et al.*, 2019), the value of incoming speed is given to the horizontal speed of raindrops. The vertical velocity and initial volume fraction of different diameters of raindrops are given according to equation (5) and equation (6), respectively.

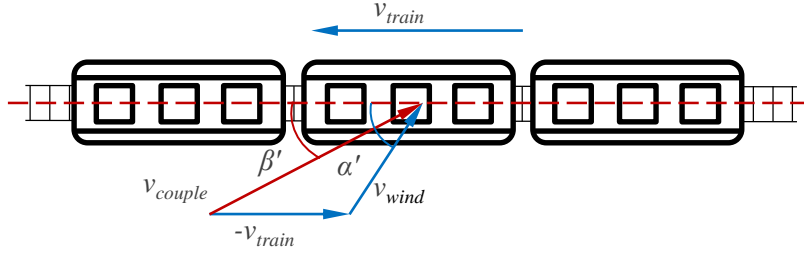


Figure 5. Parameters of coupled wind speed definition

## 2.4 Grid Generation

The domain is discretized based on an unstructured trimmer grid in STAR-CCM+ developed by Siemens. As illustrated in Figure 6(a), four refinement boxes (i.e., coarse, middle, fine, and extra-fine boxes) are used to capture detailed flow separations accurately. Due to most flow fluctuations occurring near the train's surface, the grid is finely formed in the train's complicated structure (Huang *et al.*, 2016). To evaluate the effect of mesh number, three different mesh types, including coarse (more than 10 million), medium (more than 25 million), and fine (more than 40 million) meshes, are compared. In an open-air scene with the crosswind, the side force ( $F_S$ ), lift force ( $F_L$ ), rolling moment around the leeward side rail ( $M_T$ ), are the concerned aerodynamic parameters of the train. To ensure comparability of results, the side coefficient ( $C_S$ ), lift force coefficient ( $C_L$ ), and the rolling moment coefficient ( $C_M$ ), are used to compare the sensitivity of the meshing strategy and are respectively defined as:

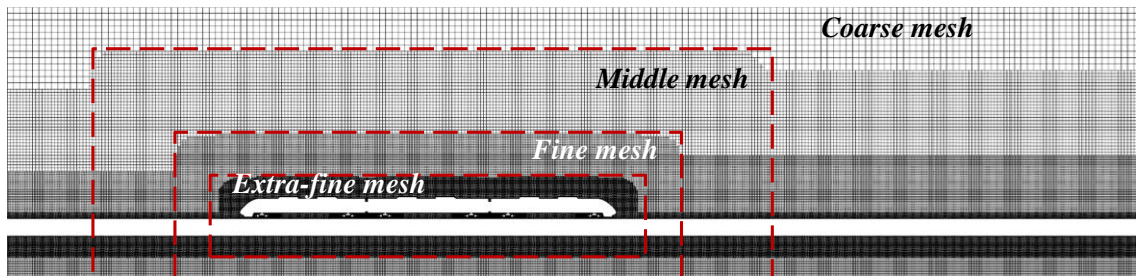
$$C_S = F_S / (0.5\rho v_{couple}^2 A) \quad (8)$$

$$C_L = F_L / (0.5\rho v_{couple}^2 A) \quad (9)$$

$$C_M = M_T / (0.5\rho v_{couple}^2 Al) \quad (10)$$

where,  $A$  is the reference area, which is the projected area of the train's cross-section and is 11.22 m<sup>2</sup> for the full-scale size;  $l$  is the reference length, which is 3 m for a full-scale size (EN14067-6, 2010);  $\rho$  is the air density and is equal to 1.225 kg/m<sup>3</sup>;  $v_{couple}$  is the synthetic wind speed of train's running speed and crosswind speed, which is defined as shown as Figure 5.

(a)



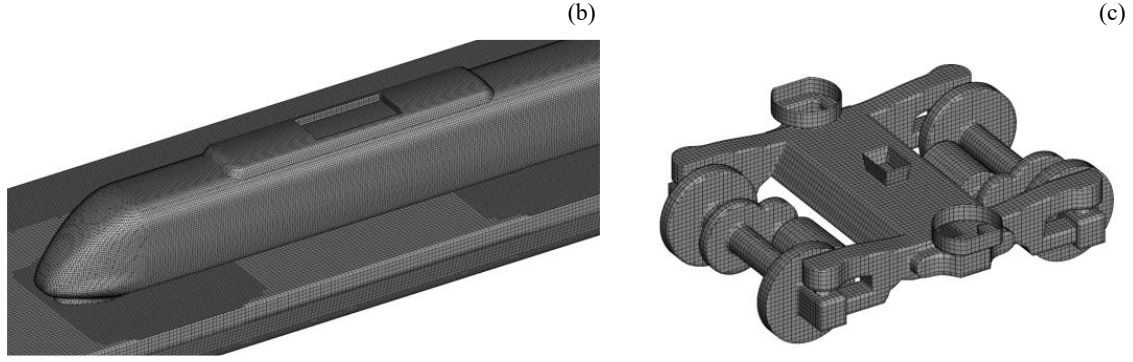


**Figure 6.** The computational mesh: (a) mesh of the refinement region, (b) mesh of train surface, and (c) mesh of bogie surface.

Table 1 compares the aerodynamic loads coefficient for each mesh strategy. The train's aerodynamic loads coefficient shows a less than 5% discrepancy between the meshing strategy of coarse and medium, while less than 1% difference was recorded between the meshing strategy of medium and fine. The compared results suggest that the medium mesh strategy can match the requirements of the engineering application. Figure 6(b) and (c) show the surface grid by using the strategy of medium mesh. Furthermore, according to the turbulence model used in the current work,  $y^+$  distribution on the surface of the train complies with its requirement, which are in the ranging from 30 to 150.

**Table 1.** Compared results of aerodynamic loads coefficient for different mesh strategy

Mesh strategy	Mesh number	$C_S$	$C_L$	$C_M$
Coarse	11,291,355	0.826	0.135	-4.658
Medium	25,742,966	0.806	0.128	-4.555
Fine	40,281,614	0.799	0.126	-4.516

## 2.5 Solver settings

Based on previous studies on trains running on viaducts under crosswind scenarios, most train-related flow fields can be observed with turbulent features. A turbulence model, therefore, was applied in the current work. At the operating speed of 200 km/h, the maximum speed on the Chinese intercity railway, the corresponding Mach number (Ma) is calculated and is less than 0.3. Following the work, the air is assumed to be viscous and incompressible, according to Anderson (2010). Owing to the benefit of reducing computing consumption, good stability for the solution and more accurate mimicking of the flow physics near the wall boundaries (Xie *et al.*, 2014; Chitrakar *et al.*, 2017; Kummitha *et al.*, 2021), the standard  $k-\epsilon$  turbulence model with enhanced wall treatment is adequate for modeling large-scale flow near trains or other complex structures under crosswind conditions (Li *et al.*, 2011b; Liu and Zhang, 2013; Zhang *et al.*, 2017). Furthermore, according to the previous investigations, a high agreement is shown between the measured data and the numerical results, when the standard  $k-\epsilon$  model is used for simulating the turbulence transport under the

wind-driven rain environment (Kubilay *et al.*, 2013; Pettersson *et al.*, 2016). Thus, the steady standard  $k-\varepsilon$  turbulent model is employed in this work.

In addition, the environment with crosswind and raindrops is a multiphase flow, since it consists of different phases. The Discrete Particle Model (DPM) and Eulerian Multiphase Model (EM model) are the two most common multiphase flow models, which are often used in conjunction with turbulent models, used to simulate complex fluid flows involving multiple phases. In the process of mimicking the wind and rain environment, the turbulent model provides information about the turbulence and flow structures, which is then used to calculate the interphase exchange terms in multiphase flow models. The coupling between the turbulent model as well as the multiphase flow model is achieved through the exchange of information about the velocity, turbulence, and other flow properties between the models at each iteration step of the simulation. The wind phase in DPM is solved using the Eulerian method, while raindrops are tracked by the Lagrangian method (Yu *et al.*, 2021). The EM model, according to the physical properties and dynamic reactions, classifies air and raindrops of varying diameters as different phases (Stark and Fritsching, 2015; Rane and He, 2020), and solves the governing equation of each phase (ANSYS, 2011). Due to the aerodynamic performance of trains on viaducts would be substantially impacted by the turbulent transport of raindrops particles with discontinuous characteristics, the EM model, which can examine the influence of raindrops' motion on complicated structures under the action of turbulent transport (Shao *et al.*, 2011), is adopted herein.

The turbulence model and multiphase flow model used in this paper are described above. Besides, the commercial software Fluent is used to conduct the numerical simulations with the finite volume method (FVM), and the Green-Gauss Cell-Based method is employed to calculate gradients in the control volumes. The pressure-based incompressible solver is adopted, and the Phase Coupled Semi-Implicit Method for Pressure Linked Equations (SIMPLE) algorithm (Shao *et al.*, 2011) is employed to solve the pressure and velocity coupling equations. The second-order upwind technique is used to discretize the turbulent kinetic energy and turbulent dissipation rate (Huang and Li, 2010).

### **3 Validation of numerical results**

Comparison with experimental results is an important tool to validate the accuracy of numerical calculations. However, conducting a full-scale test or a wind tunnel test regarded to trains and complex structures is still a tough challenge under the existing experimental conditions. For this reason, two cases measured in the wind tunnel and reported previously are employed to validate the numerical method used in the current study. In Section 3.1, the aerodynamic force coefficients of the train suffered the wind force solely are compared with the experimental results, to validate the accuracy of the numerical approach used to model the flow field surrounding the train or complex structures. Besides, in Section 3.2, the comparison of the aerodynamic load coefficients of the aerofoil under wind and rain coupled action was given to validate the numerical approach employed to simulate the wind and rain environment.

### 3.1 Comparison between numerical and wind tunnel test results under crosswind-only

The wind tunnel experiment conducted by Zhang *et al.* (2018), which was reported previously, is utilized to confirm the feasibility of the numerical approach used to simulate the flow field around the train. A wind tunnel with a cross-section of  $8\text{ m} \times 6\text{ m}$  was used to test the 1:8 scaled model that combined three cars, and the six-component balances were employed in this experiment. To ensure the reliability of the comparison, the calculation field and boundary conditions setting depends on the actual situation of the wind tunnel test section, including wind speed, yaw angle and placed model, and more details can be found in Zhang *et al.* (2018). Additionally, the mesh strategy, and solver settings are the same as indicated previously. According to the velocity of the incoming flow, the train's height and kinematic viscosity used in the experiment, the Reynolds number of the wind tunnel test is calculated as  $1.89 \times 10^6$ .

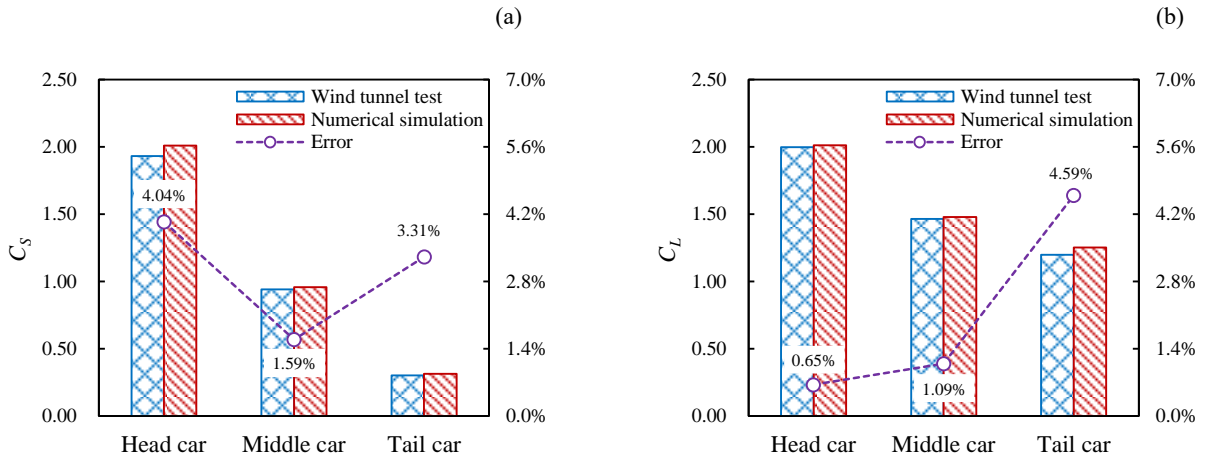


**Figure 7.** Numerical result validations with the wind tunnel test: (a)  $C_S$ ; and (b)  $C_L$ .

Since the side force coefficient and lift force coefficient is of high interest in this study, the  $C_S$  and  $C_L$  obtained in the numerical simulations and wind tunnel tests are compared and illustrated in Figure 7. The highest  $C_S$  and  $C_L$  difference between the findings of the numerical simulations and the wind tunnel tests are both less than 5%, showing that the numerical method employed in this study was suitable for future CFD analysis. Moreover, flow structures dominate the train's aerodynamic forces in practice, which indirectly proves the reliability of the flow structure analysis in this study is reliable (Chen *et al.*, 2019b).

### 3.2 Comparison between numerical and wind tunnel test results under wind and rain

An experiment using aerofoil NACA 64-210 under the coupled wind and rain action, which was previously undergone in the NASA wind tunnel (Bezous *et al.*, 1992), is utilized to validate the numerical method used in the current work. The test segment has a cross-sectional area of  $14\text{ ft} \times 22\text{ ft}$  ( $4.27\text{ m} \times 6.71\text{ m}$ ), and detailed information are shown in the wind tunnel test schematic diagram performed in Figure 8(a). Considering the comparability of results, the characteristic dimensions of the wind tunnel, the model and apparatus placement, as well as the initial parameters of incoming flow and rain phase, were used to determine

the computational domain and boundary condition for the simulations, but the computational technique, mesh design, and other pertinent settings are kept consistent with that mentioned afore.

Figure 8(b) shows the compared results of the aerofoil drag coefficient as measured in the experiments and calculated using the numerical simulation in the strong rain circumstances. A gradual increase tendency is illustrated with the attack angle increase. Discrepancies between the numerical results and test results can be found at high attack angles, due to the placed holder and end plates for fixing the test model are not considered in the calculational model. Besides, the placed rain manifold also would affect the incoming flow suffered by the aerofoil model. However, within the numerical simulations and wind tunnel test, a similar increasing trend is recorded with the increase in attack angle in the rain situations. Also, the numerical simulation results match the experiment results at lower attack angles of the aerofoil, which, therefore, indicates the turbulence model and the multiphase model utilized herein are reasonable and acceptable.

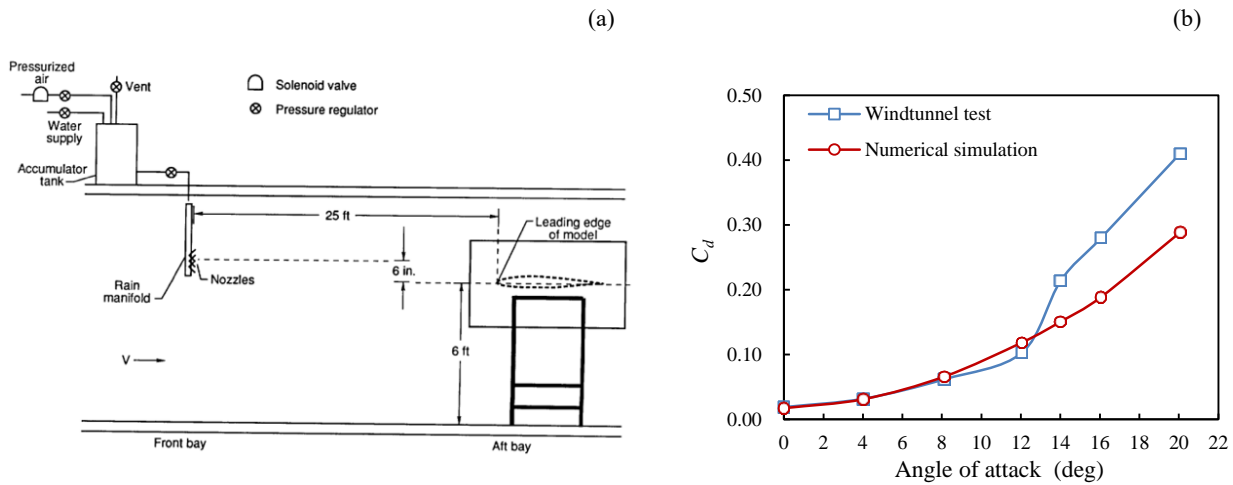


**Figure 8.** Comparison between numerical and wind tunnel test results under wind and rain: (a) schematic of the wind tunnel (adapted from Bezos *et al.* (1992)); and (b) compared results of aerofoil aerodynamic drag.

## 4 Results and discussions

### 4.1 Crosswind speed effect on the flow field surrounding the train on the viaduct

Figures 9 and 10 show the distribution of airflow and raindrops streamlines around the train and viaduct with a wind speed increase, in the train speed of 200 km/h and rainfall of 60 mm/h. Airflow around the leeward side of the train and viaduct is gradually acute along the longitudinal direction. To avoid the influence of the train's streamlined head, the cross-section of the tail car in the center of the longitudinal direction is adopted to analyze. As shown in Figure 9(a), under the action of crosswind, airflow flows along the windward side surface separates at the roof and bottom of the train, respectively, and two vortices V1 and V2 are formed on the leeward side of the train. Meanwhile, a vortex V3 is observed near the leeward side of the viaduct, owing to the obstruction of the airflow by the viaduct. With the wind speed rises, the velocity magnitude of the airflow around the train and viaduct shows an accelerated trend. As shown in Figure 9(b), four vortices are

observed under 20 m/s crosswind speed, including V4–V7. The location and scale of the vortices demonstrate a noticeable discrepancy with that shown in the 10 m/s crosswind speed. The eddy scale of V5 and V6 stretch and fall off on the train’s leeward side caused by the induction of the wind speed increases, and the newly formed vortex V4 and developed vortex V7 are closer to the structure caused by the airflow suction. As the crosswind speed increases to 30 m/s, as shown in Figure 9(c), the trend of vortex stretching becomes further obvious. The scale of vortices V8, V9 and V11 around the train and viaduct demonstrates an expand tendency, and the fall-off vortex shows a reduced scale tendency, such as V10 shown in Figure 9(c).

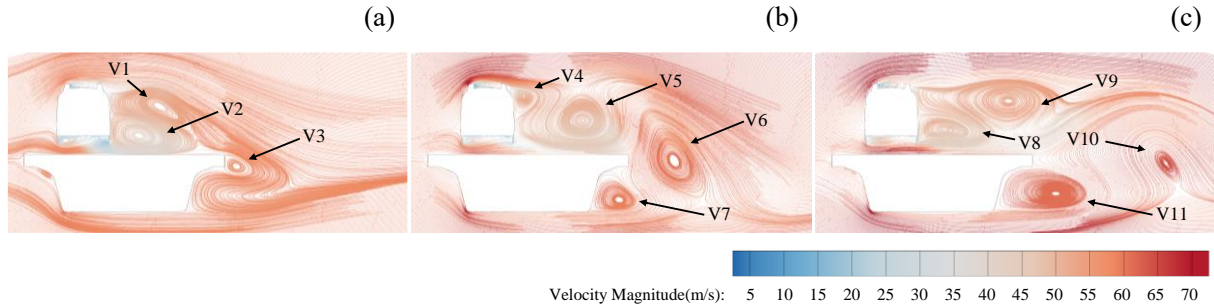


**Figure 9.** Airflow streamlines around the train and viaduct with different crosswind speeds: (a) 10 m/s, (b) 20 m/s, and (c) 30m/s

Due to the characteristic of the EM model, the different diameters of raindrop distribution in the flow field can be analyzed. According to the grouping interval described in Section 2.2.2, to analyze the flow discrepancy between small and large diameter raindrops in the wind and rain field, streamlines of different particle diameter raindrops in the flow field are utilized to compare. The streamlines of raindrops with a diameter of 0.25 mm and 1.25 mm in different wind speeds are plotted in Figure 10. Compared with the airflow streamlines shown in Figure 9, the distribution of raindrops’ streamlines demonstrates a similar feature to that of air under the same crosswind speed. Three vortices  $V_{r1}$ ,  $V_{r2}$ , and  $V_{r3}$  emerge in the distribution of 0.25 mm raindrops’ streamlines at approximate positions on the leeward side, compared to that of airflow streamlines, while two vortices  $V_{r1'}$  and  $V_{r2'}$  appear in that of 1.25 mm raindrops’ streamlines, as demonstrated in Figures 10(a) and (d), respectively. Owing to the effect of the viaduct deck and the vortices scale of the airflow, the raindrops vortices  $V_{r1}$  and  $V_{r2}$  formed on the leeward side are significant and hold an expanding tendency by the inertia effect of raindrops. However, in the combined influence of small-scale vortex of airflow and gravity, an adverse impact of formed vortices is observed, and the producing of raindrops’ vortex  $V_{r3}$  is weak on the viaduct’s leeward side. Due to the influence of gravity becoming increasingly significant, this phenomenon appeared in the large-diameter raindrops demonstrates prominently, while the velocity of the large-diameter raindrops demonstrated a reducing trend. As the crosswind speed increases, the distribution of raindrops streamlines shows a similar regularity, as shown in Figure 10. Due to the developing and expanding of vortices formed on the leeward side of the train, the smaller vortices  $V_{r4}$  and  $V_{r4'}$ , as shown in Figures 10(b) and (e), gradually decrease in size and merge into the larger vortices  $V_{r5}$  and  $V_{r5'}$  under the effect of winding and sucking. And vortices  $V_{r6}$  and  $V_{r7}$  formed by small diameter raindrops

demonstrate expanding trends since its greater inertial force compared to air, while the effect of gravity is more pronounced for the large particles of raindrops at open sites, as shown in Figure 10(e). Besides, as the crosswind speed increases, the negative pressure region at the leeward side of the train expands obviously, which causes the velocity of raindrops to demonstrate a reducing trend in both small and large particles of raindrops. The scale of vortices formed by small particles of raindrops is approximately equal to airflow, and large particles of raindrops show a notable dropping trend by the combination with inertial impact, as shown in Figures 10(c) and (f). Further, due to airflow accelerating in the underbody area and accessing the lower velocity motion region of the large-size raindrops, as shown in Figure 8(f), a small-scale vortex is rebuilt in region A.

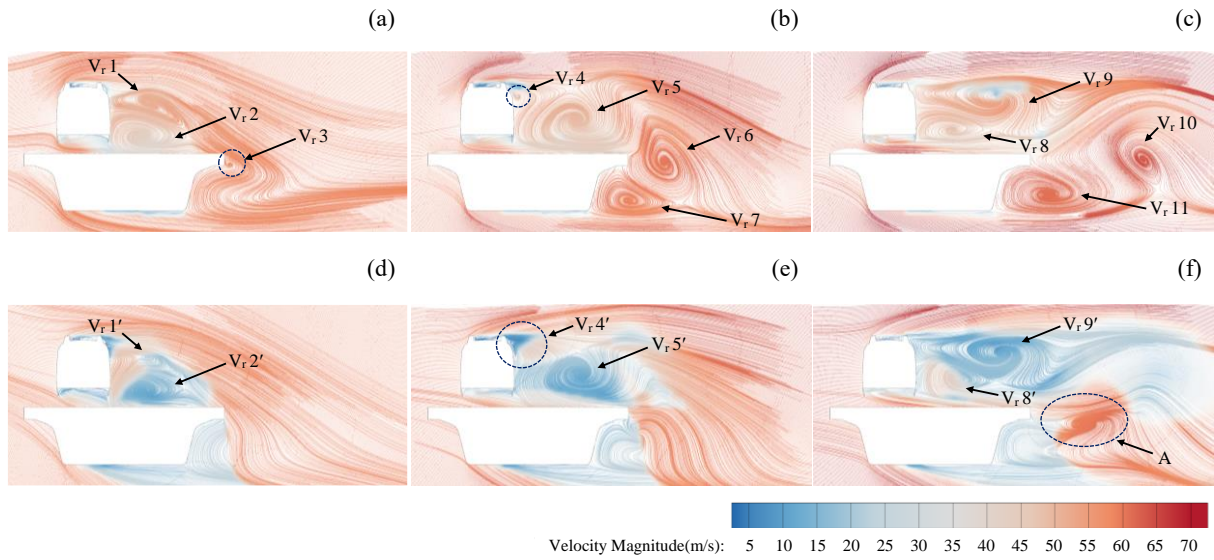


**Figure 10.** Streamlines distribution of raindrops with different diameters and crosswind speeds: (a) 0.25 mm and 10 m/s, (b) 0.25 mm and 20 m/s, (c) 0.25 mm and 30 m/s, (d) 1.25 mm and 10 m/s, (e) 1.25 mm and 20 m/s, and (f) 1.25 mm and 30 m/s

#### 4.2 Coefficients of aerodynamic load for the train at varying crosswind speeds

Figure 11 shows the tendency of aerodynamic force coefficients of the train variation with wind speed increase in the operational speed of 200 km/h and rainfall of 60 mm/h. As shown in Figures 11(a), (b) and (c),  $C_S$ ,  $C_L$  and  $C_M$  of the head car, middle car and tail car rise dramatically with the increasing crosswind speed. The  $C_S$  and  $C_M$  of the head car are more significant than that of the middle car and tail car, and the discrepancy between the head car, middle car and tail car becomes more extensive with the crosswind increase. For the  $C_L$ , however, the difference between each carriage is unobvious with the growing crosswind speed, especially the middle car and tail car.

Moreover, Figure 11 also displays the percentage difference between rain and no-rain circumstances. Figures 11(a) and (c) indicate that the  $C_S$  exhibits the same trend as the  $C_M$  when comparing the rain and no-rain scenarios, and that the difference narrows as the crosswind increases. Compared to no-rain conditions, the growth rate of  $C_S$  and  $C_M$  of the tail car is the largest in most situations, and the middle car is the least in all

cases. This is probably because the action of crosswind enhances and occupation of raindrops' impact weakens with increasing crosswind speed. Meanwhile, as shown in Figure 11(b), the  $C_L$  of each car exhibits indistinct differences, especially the middle car and tail car, caused by the probable reason that the airflow separation near the train becomes apparent, and the raindrops are affected by the airflow and thrown away along the windward side surface of the roof towards the leeward side, weakening the effect on the train in the vertical direction. Furthermore, the larger pressure pulsation is created beneath the streamlined head of the head car, since the effect of crosswind is smaller than the slipstream caused by the train at a lower speed. It, therefore, causes the impact of raindrop increases, and the difference between the rain and no-rain scenario is rather large in  $C_L$  of the head car under the 10 m/s of crosswind speed.

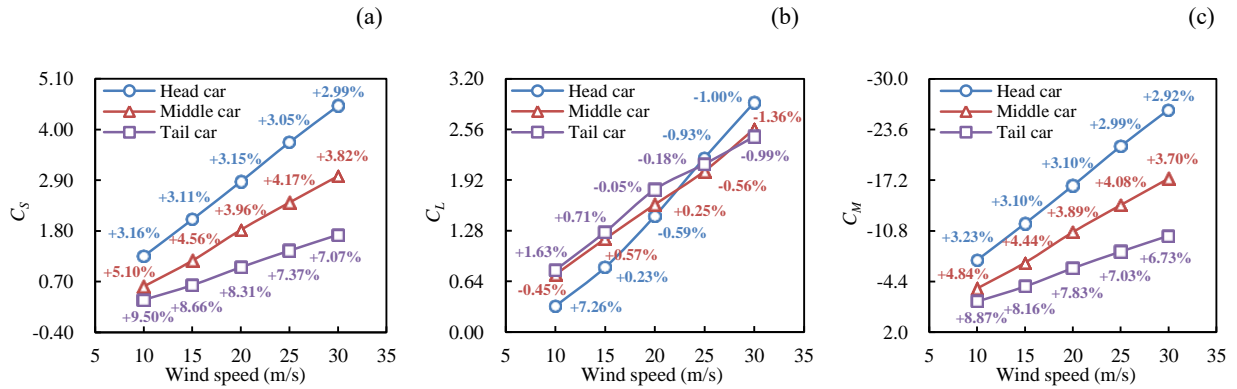


Figure 11. Comparison of aerodynamic force coefficients between head car, middle car and tail car: (a)  $C_s$ , (b)  $C_L$  and (c)  $C_M$ .

As analyzed above, the aerodynamic forces of the head car are the most significant. To further investigate the variation of  $C_s$ ,  $C_L$  and  $C_M$  with the growing crosswind speed at different operational speeds of the train, the head car is adopted to analyze. Under the action of 60 mm/h rainfall, the aerodynamic load coefficients of the head car with different crosswind speeds and train speeds are plotted in Figure 12. The  $C_s$  and  $C_M$  both demonstrate the increasing trend with crosswind speed growing at different operational speeds of the train, as shown in Figures 12(a) and (c). With the same operating speed, as shown in Figure 12(b), the  $C_L$  shows a rising trend as the crosswind speed increase. Likewise, the  $C_L$  increases as train speed decrease with crosswinds of 10–20 m/s or increases with crosswinds of 20–30 m/s.

(a) (b) (c)

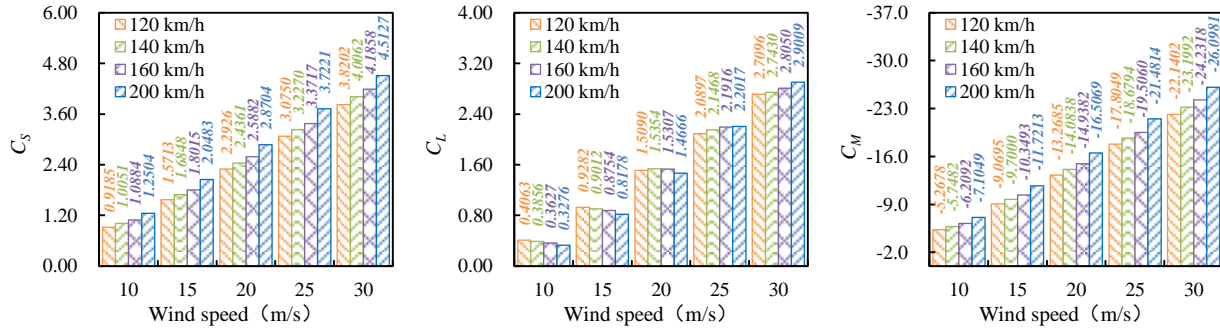


Figure 12. Comparison of aerodynamic force coefficients with different operational speeds of the train: (a)  $C_s$ , (b)  $C_L$  and (c)  $C_M$ .

### 4.3 Rainfall effect on the flow field surrounding the train on the viaduct

The streamlines distribution of 0.25 mm and 1.25 mm diameter raindrops in different rainfalls are plotted in Figure 13, as crosswind and operating speeds are the same. Compared with the scenario shown in Figures 10(b) and (e), the streamlines distribution of raindrops diameter particles of 0.25 mm and 1.25 mm demonstrate a similar tendency. Additionally, the distribution of streamlines shows non-obvious alteration with an increase in rainfall, most likely owing to the fact that the influence of crosswinds is predominant while raindrops operate as supplementary effects in the flow field. Under the coupled action of wind and rain, because of the separation of the airflow and the obstacle of the train and viaduct, most raindrops are blown by airflow and hurled outward from the train's roof and viaduct's bottom. However, with the rainfall increase, the movements of some raindrop particles on the train's leeward side show subtle differences, owing to the perturbation of the flow field by raindrop particle motion. As shown in Figure 13, the velocity of raindrops in region B near the vortex  $V_{r4}$  and  $V_{r4}'$  demonstrates a rising tendency as the rainfall increases, and the vortex  $V_{r4}$  demonstrates a trend of decreasing scale. This is probably because the continuous distribution of airflow can easily cross from the interval of raindrop particles, but fewer raindrops could be driven by the airflow, as the raindrop particles show a significant discrete distribution in the case of the lower volume fraction of raindrops in the light rain. With the dense distribution of raindrop particles at high rainfall, the movement of raindrop particles is intensified by continuous airflow, while the velocity of raindrops demonstrates an increasing trend.

In addition, by the influence of this regularity and the rainwater accumulation on the viaduct deck, the variation of raindrops velocity distribution in region C also shows an accelerated tendency of movement with increasing rainfall, and the variation in the region near the viaduct deck becomes more significant owing to the unevenness, as shown in Figures 13 (a), (b) and (c). Besides, the number of raindrop particles diffused in the air increases significantly with the increase of rainfall, which increases the hindrance effect of the airflow and weakens the formation of turbulent vortices. Thus, with the rainfall increasing, the scale of the vortex  $V_{r5}$  demonstrates a decreasing trend, especially in the large-scale size raindrops particles, while the scale size  $D_p$  of

vortex  $V_{r5}$  also indicates a diminishing scale tendency, as shown in Figures 13(d), (e) and (f). This feature is also manifested in region D shown in Figure 13, which is away from the train's leeward side.

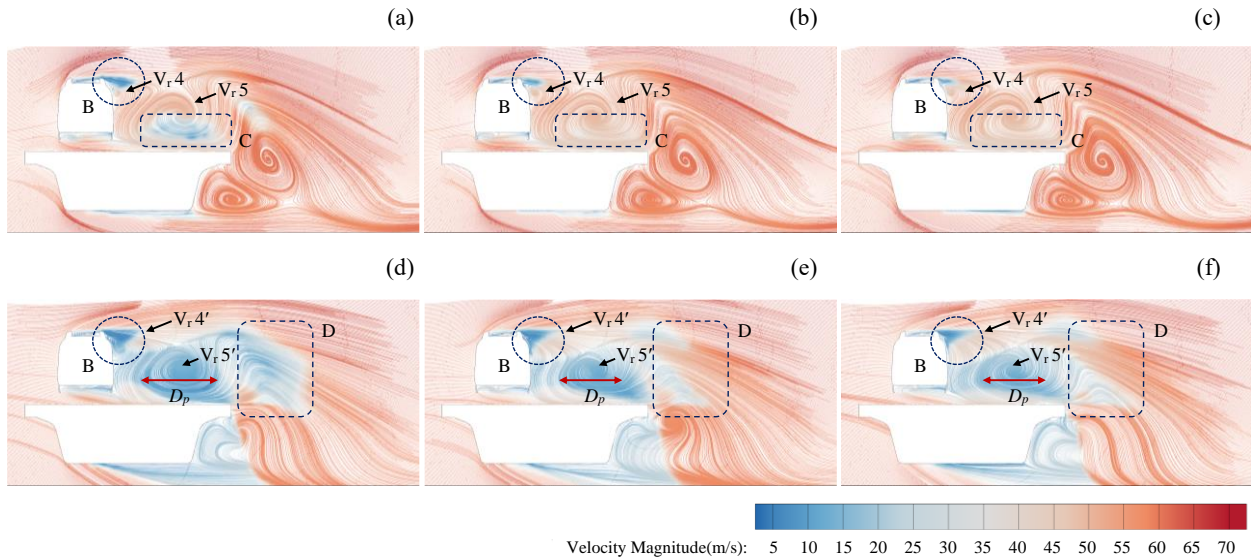


**Figure 13.** Streamlines distribution of raindrops with different diameters and rainfalls: (a) 0.25 mm and 20 mm/h, (b) 0.25 mm and 60 mm/h, (c) 0.25 mm and 100mm/h, (d) 1.25 mm and 20 mm/h, (e) 1.25 mm and 40 mm/h, and (f) 1.25 mm and 100 mm/h

#### 4.4 Coefficients of aerodynamic load for the train at varying rainfall

Figure 14 shows the variation of the aerodynamic force coefficient of the train change with rainfall growing at the operational speed of 200 km/h and crosswind speed of 20 m/s. As shown in Figures 14(a) and (c),  $C_S$  and  $C_M$  of the head car, middle car and tail car grow slightly with the increase in rainfall, and the percentage discrepancy is also plotted in the figure compared with the no-rain condition. The quantity of droplets in the flow field grows considerably as rainfall increases, causing a violent impact on the side of the train. Therefore, discrepancies between no-rain and rain scenarios become more significant with the rising rainfall, especially  $C_S$  and  $C_M$ . In addition,  $C_L$  shows a slightly dropping trend with the increase of rainfall, owing to the number of raindrops increasing in the vertical direction and impacting the top surface of the train. However, the discrepancy of  $C_L$  between rain conditions and no-rain conditions is indistinguishable because the driven action of airflow plays the dominant status in the wind and rain environment.

(a) (b) (c)

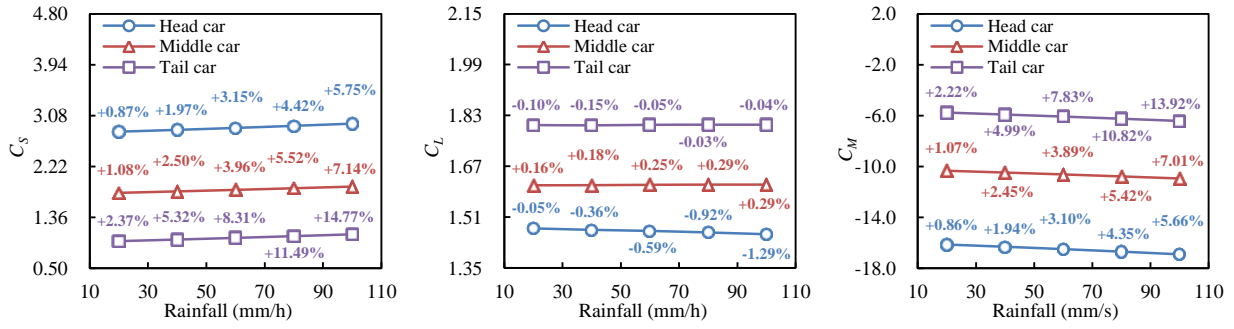


Figure 14. Comparison of aerodynamic force coefficients between head car, middle car and tail car: (a)  $C_S$ , (b)  $C_L$  and (c)  $C_M$ .

With a crosswind of 20 m/s, the aerodynamic load coefficient comparisons of the head car under various rainfalls and train operational speeds are plotted in Figure 15. The  $C_S$  and  $C_M$  both show the dropping tendency with the operational speed of the train decreasing in different rainfalls, as shown in Figures 15(a) and (c). In the aspect of  $C_L$ , however, as shown in Figure 15(b), the difference in rainfall and operating speed demonstrates an imperceptible fluctuation.

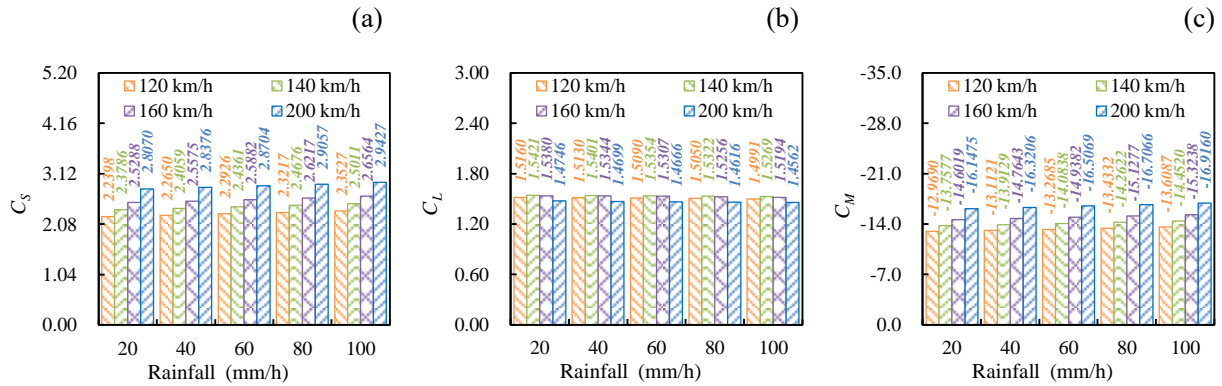


Figure 15. Comparison of aerodynamic force coefficients with different operational speeds of the train: (a)  $C_S$ , (b)  $C_L$  and (c)  $C_M$ .

#### 4.5 Computational model of multi-body dynamics

As analyzed above, the impact of crosswind is predominant on the running train under the coupled action of crosswind and raindrops. According to relevant research (Chen *et al.*, 2019a), the safety indicators of the head car are more significant than other cars of the train. Therefore, the operational stability and safety of trains are mainly limited by the head car, and the critical vehicle speed of the train is investigated by the safety indexes.

To investigate the dynamic response and safety index variation with the rising crosswind speed and rainfall at different operational speeds of the train, the aerodynamic forces and moments calculated by the numerical simulation are inputted into the multi-body dynamic model by the external excitation function. According to the Code for Design of Intercity Railway (TB10623-2014) published by the Railway Operational

Management Department of China, the operational safety can be evaluated by the index, including the derailment coefficient  $Q/P$ , the wheel unloading rate  $\Delta P/P$  and wheel-set lateral force  $p_H$ .

As the train runs at high speed, the most unfavorable combination of factors such as line condition, vehicle structure parameters and external excitation will make the train derailment chance significantly higher, which can be evaluated by the derailment coefficient as follows:

$$\frac{Q}{P_0} = \frac{\tan \alpha - \mu}{1 + \mu \tan \alpha} \quad (11)$$

where,  $Q$  donates the lateral force;  $P_0$  is the vertical force;  $\alpha$  is the wheel edge angle; and  $\mu$  donates the friction coefficient between the wheel edge and the side of the rail. The limit value of the derailment coefficient is employed by  $Q/P \leq 0.8$ .

The wheel unloading rate is defined as the ratio between the wheel unloading of the wheel on one side of the wheel  $\Delta P$  and the average static wheel load  $P$ . The safety value of the wheel unloading rate is defined as follows:

$$\Delta P / P \leq 0.60 \quad (12)$$

Also, under the impact of crosswinds and raindrops, the lateral force of the wheel-set will increase significantly. The excessive horizontal transverse force will lead to track traverse and seamless railroad dynamic instability, increasing the risk of train derailment. The safety value of wheel-set lateral force  $p_H$  is defined as follows:

$$p_H \leq 10 + \frac{p_0}{3} \quad (13)$$

where,  $p_0$  donates the static axis weight. As the axle weight of the bogie of the intercity train analyzed in this paper is 17 t, the limit value of the wheel-set lateral force is employed by  $p_H \leq 65.50$  kN.

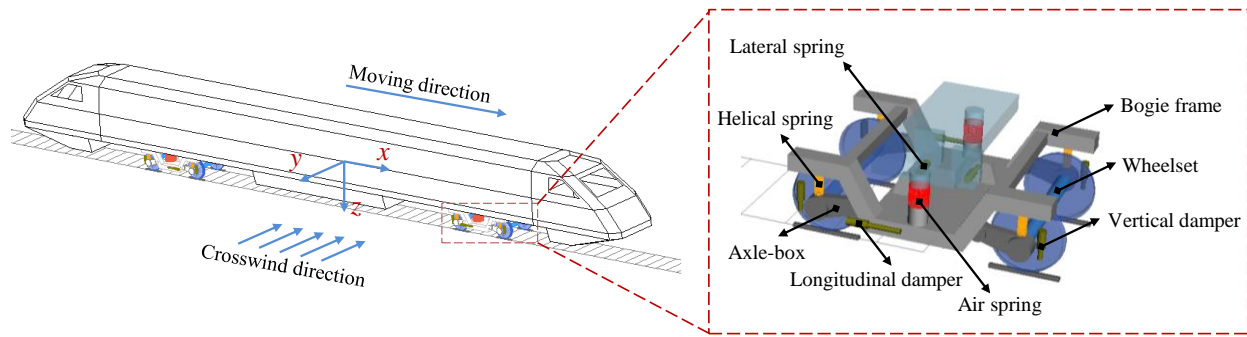


**Figure 16.** The vehicle dynamic model

To analyze the dynamic characteristic of the intercity train running on the viaduct, SIMPACK is employed to establish the multi-body dynamic model. According to previous studies (Li *et al.*, 2022b), both the railway and the viaduct experience minimal vibration during the train operation, and their self-excited

loads are also relatively small. Furthermore, crosswinds significantly affect train safety, yet their impact on viaduct vibration can be basically ignored. Based on this, the train's dynamic response is the factor of primary consideration in the current work. As shown in Figure 16, components of the train model are regarded as rigid, including a car body, two bogie frames, four wheel-set and eight axle boxes, while the car body, frame and wheel-set have six degrees of freedom (DOFs), and the axle box has one DOF. All components above link through suspension systems consisting of joints and springs-damp elements, and various non-linear factors, i.e., vertical damper, helical spring, longitudinal damper, air spring, etc., are in consideration. Besides, forces and moments caused by the action of wind and raindrops are inputted in the model, containing the side force, lift force, overturning moment, pitching moment and yaw moment (Zhao and Zhai, 2015). The wheel tread profile and the rail profile adopt the LMA tread profile and the T60 standard rail profile, respectively, and track irregularity is also considered in the model. In this simulation, the German high-speed railway track irregularity is applied, which can refer to Zhao and Zhai (2015), so the details of the railway track irregularity are not introduced again here

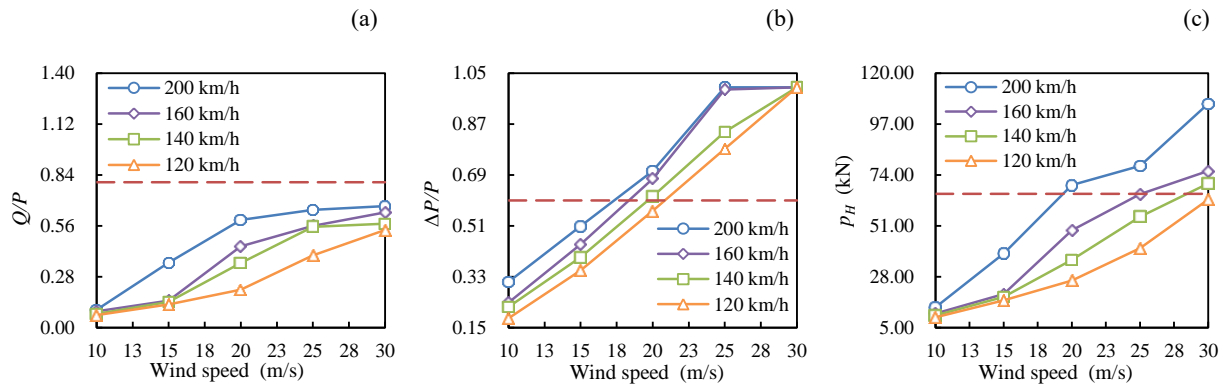


Figure 17. Comparison of safety indexes with different crosswind speeds: (a)  $Q/P$ , (b)  $\Delta P/P$ , and (c)  $p_H$

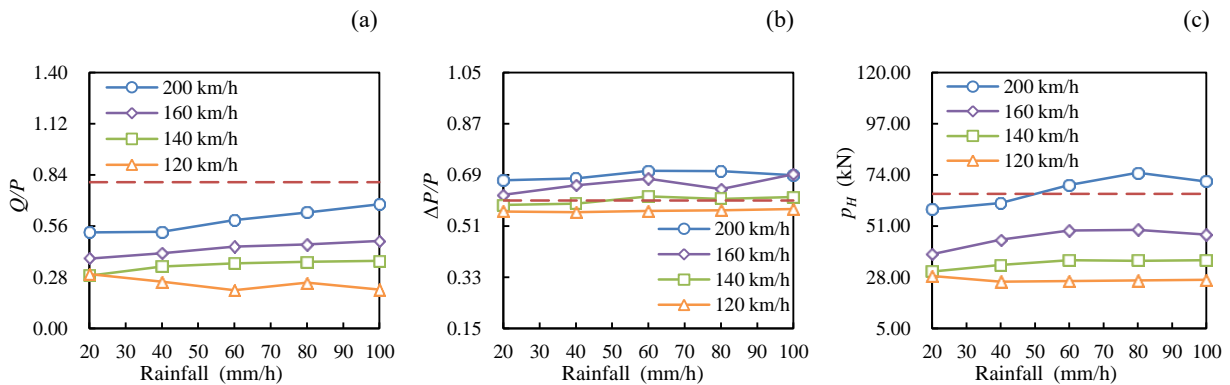
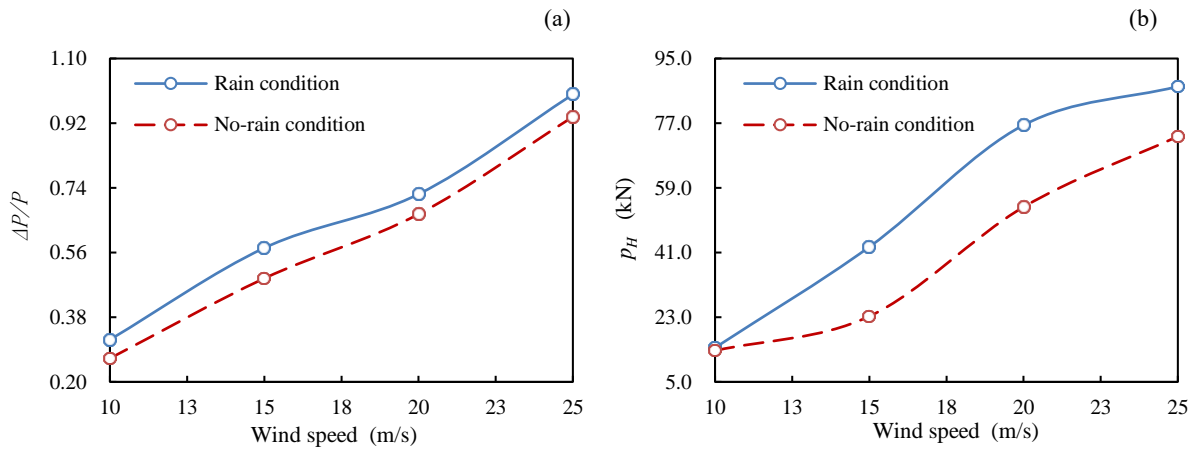


Figure 18. Comparison of safety indexes with different rainfalls: (a)  $Q/P$ , (b)  $\Delta P/P$ , and (c)  $p_H$

The variation of indexes with the growth of crosswind speed and rainfall are plotted in Figures 17 and 18, and the dashed line, where, is the limited value of safety indexes. As indicated in Figures 17(a), (b), and (c), as the crosswind speed increase, indexes of  $Q/P$ ,  $\Delta P/P$  and  $p_H$  exhibits an increasing tendency within the same operating speed and rainfall, while a slight fluctuation with the growth of rainfall was observed, which are presented in Figures 18(a), (b), and (c). However, there is a noticeable soar trend of  $Q/P$ ,  $\Delta P/P$  and  $p_H$  with the increase in operational speed of the train.

#### 4.6 Operational safety characteristics of the train on the viaduct

As shown in Figures 17 and 18, the  $Q/P$  is lower than the safety index limitation, while the  $\Delta P/P$  and  $p_H$  in certain situations exceed the critical values. Thus, the critical vehicle speed of the train speed should be analyzed based on the critical values of  $\Delta P/P$  and  $p_H$ . Besides, due to indexes of  $\Delta P/P$  and  $p_H$  showing an unobvious fluctuation with the variation of rainfall, the safety indexes change with crosswind speed is adopted to analyze the critical crosswind speed under different rainfalls and running speeds of the train. As shown in Figures 19(a) and (b), the variation of  $\Delta P/P$  and  $p_H$  change with crosswinds between rain conditions (100 mm/h) and no-rain conditions show a significant discrepancy, owing to the fact that raindrops are constantly hitting the train's surface.



**Figure 19.** Comparison of safety indexes of the train: (a)  $\Delta P/P$  and (b)  $p_H$

Based on the method of cubic polynomial fitting, the critical crosswind speed that the train can tolerate at the different running speeds of the train can be obtained, as an example plotted in Figure 20. Under the rainfall of 60 mm/h, the safety region obtained from different indicators demonstrates the discrepancy, while the critical crosswind speeds obtained based on the judgment of  $\Delta P/P$  are much lower than that of  $p_H$ , as shown in Figure 21. Thus, under the coupled action of crosswind and raindrops, utilizing  $\Delta P/P$  to determine the critical crosswind speeds that the train on the viaduct can endure would be conservative and safe.

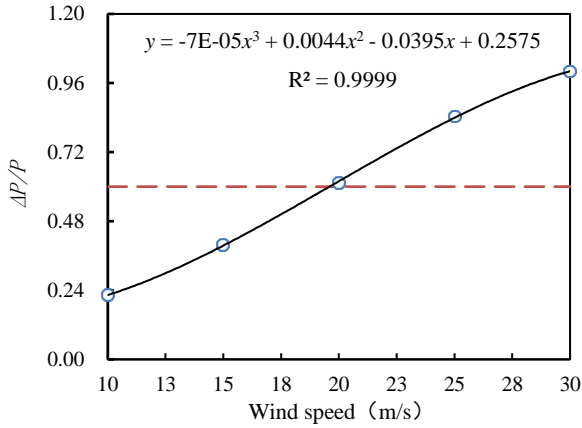


Figure 20. Fitting curve of  $\Delta P/P$  in a certain situation

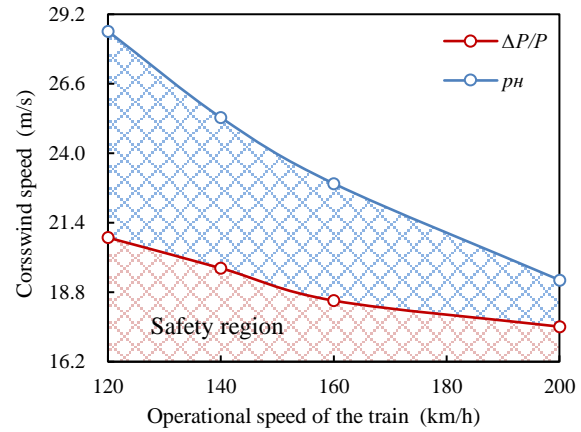


Figure 21. Comparison of the safety region of the train

The fitting surface of the coupling relationship between crosswind speed-rainfall amount-critical train speed is shown in Figure 22. Under lower crosswind speeds, rainfall obviously affects the critical operating speed. However, the train's critical operating speed shows a significant decline when the crosswind increase, which demonstrates that the influence of crosswind speed on the operating safety of intercity trains running on viaducts is more prominent than rainfall intensity performance.

Based on the critical crosswind speed in different operational speeds of the train, the operating safety region of the train running on the viaduct can be obtained by the method of cubic polynomial fitting in different rainfalls. As shown in Figure 23, there are discrepancies between the risings of rainfall based on the judgment of  $\Delta P/P$ . The critical crosswind that the train can tolerate running on the viaduct show a decreasing tendency with the operating speed rising, while increased rainfall also results in dropping trends in the safety region. In the 120–200 km/h operating speed range of the train, compared to the no-rain condition, the operating safety region of the train decreased by 0.56%, 1.56%, 4.80%, 5.92% and 7.03%, respectively, in the rainfall of 20, 40, 60, 80 and 100 mm/h.

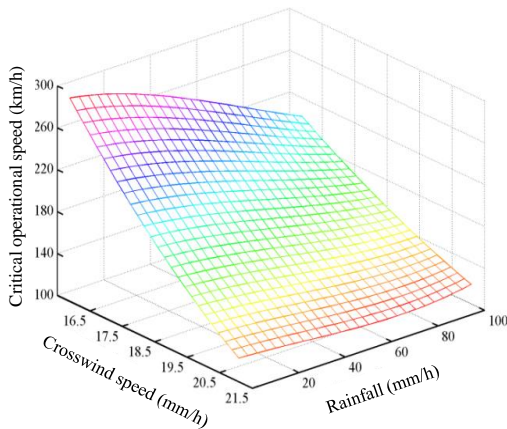


Figure 22. Fitting surface of crosswind speed-rainfall amount-critical train speed

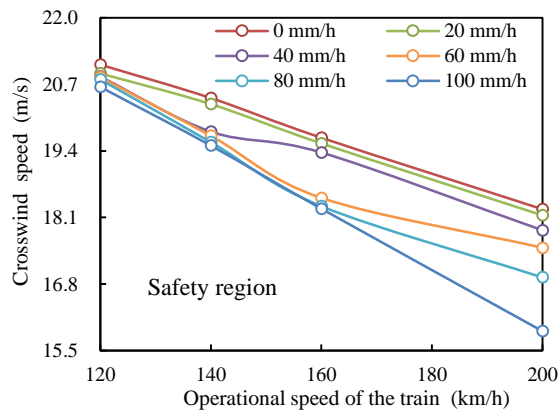


Figure 23. The train safety region in various rainfall scenarios

## 5 Conclusion

To explore the operational safety of intercity railways in metropolitan areas, the impact of crosswind speeds and rainfall on the train's aerodynamic safety is studied, including the flow field surrounding the train and viaduct, aerodynamic loads coefficients suffered by the intercity train as well as the operating safety region of intercity trains, based on the established aerodynamic model and multi-body dynamic model. The following conclusions are drawn from the numerical results.

(1) Due to raindrops being driven by the crosswind, the streamlines of raindrops surrounding the train and viaduct are comparable to airflow in the wind and rain circumstance, and both wind and rain flow structure varies significantly with the soar of crosswind speed, but its sensitivity to rainfall intensity is relatively weak.

(2) With the increase of wind speed and rainfall, the aerodynamic loads of the train show an increasing trend in different operational speeds of the train, but the discrepancy between rainfalls increasing is not greatly significant, because the impact of crosswind is predominant while raindrops operate as supplementary effects in the flow field.

(3) Based on the safety indexes of the train, in the 120–200 km/h operating speed range of the train, compared with that of no-rain conditions, the operating safety region of the train decreased by 0.56%, 1.56%, 4.80%, 5.92% and 7.03%, respectively, in the rainfall of 20, 40, 60, 80 and 100 mm/h.

This study aimed to investigate the impact of crosswinds and raindrops on intercity trains that operate on viaducts, with the goal of ensuring the safe operation of intercity railways in metropolitan areas. The focus of future research will be given on the transient calculations to capture flows of airflow and raindrops in a more realistic state, as well as the influence of different turbulent models and train operating schemes, etc.

## Reference

- Anderson, J.D. (2010), *Fundamentals of aerodynamics*. McGraw-Hill Education.
- ANSYS (2011), *Fluent 14.0 Theory Guide*.
- Avila-Sanchez, S., Lopez-Garcia, O., Cuerva, A. and Meseguer, J. (2017), "Assesment of the transverse galloping stability of a railway overhead located above a railway bridge", *International Journal of Mechanical Sciences*, Vol. 131, pp.649-662.
- Baker, C. and Sterling, M. (2018), "The calculation of train stability in tornado winds", *Journal of Wind Engineering and Industrial Aerodynamics*, Vol. 176, pp.158-165.
- Bezos, G.M., Dunham, R.E., Gentry, G.L. and Melson, W.E., 1992. Wind tunnel aerodynamic characteristics of a transport-type airfoil in a simulated heavy rain environment.
- Bian, X., Jiang, H., Cheng, C., Chen, Y., Chen, R. and Jiang, J. (2014), "Full-scale model testing on a ballastless high-speed railway under simulated train moving loads", *Soil Dynamics and Earthquake Engineering*, Vol. 66, pp.368-384.
- Chen, C., Zhang, H., Feng, C., Xuan, Y., Qian, T. and Xie, J. (2022a), "Analysis of wind-driven rain characteristics acting on building surfaces in Shanghai based on long-term measurements", *Journal of Building Engineering*, Vol. 45, pp.103572.

Chen, J., Gao, G. and Zhu, C. (2016), "Detached-eddy simulation of flow around high-speed train on a bridge under cross winds", *Journal of Central South University*, Vol. 23 No. 10, pp.2735-2746.

Chen, Z., Liu, T., Jiang, Z., Guo, Z. and Zhang, J. (2018), "Comparative analysis of the effect of different nose lengths on train aerodynamic performance under crosswind", *Journal of Fluids and Structures*, Vol. 78, pp.69-85.

Chen, Z., Liu, T., Li, M., Yu, M., Lu, Z. and Liu, D. (2019a), "Dynamic response of railway vehicles under unsteady aerodynamic forces caused by local landforms", *Wind and Structures*, Vol. 29 No. 3, pp.149-161.

Chen, Z., Liu, T., Li, W., Guo, Z. and Xia, Y. (2021), "Aerodynamic performance and dynamic behaviors of a train passing through an elongated hillock region beside a windbreak under crosswinds and corresponding flow mitigation measures", *Journal of Wind Engineering and Industrial Aerodynamics*, Vol. 208, pp.104434.

Chen, Z., Liu, T., Yan, C., Yu, M., Guo, Z. and Wang, T. (2019b), "Numerical simulation and comparison of the slipstreams of trains with different nose lengths under crosswind", *Journal of Wind Engineering and Industrial Aerodynamics*, Vol. 190, pp.256-272.

Chen, Z., Rui, E., Liu, T., Ni, Y., Huo, X., Xia, Y., Li, W., Guo, Z. and Zhou, L. (2022b), "Unsteady Aerodynamic Characteristics of a High-Speed Train Induced by the Sudden Change of Windbreak Wall Structure: A Case Study of the Xinjiang Railway", *Applied Sciences*, Vol. 12 No. 14, pp.7217.

Chitrakar, S., Thapa, B.S., Dahlhaug, O.G. and Neopane, H.P. (2017), "Numerical and experimental study of the leakage flow in guide vanes with different hydrofoils", *Journal of Computational Design and Engineering*, Vol. 4 No. 3, pp.218-230.

Coelho, G.B. and Henriques, F.M. (2016), "Influence of driving rain on the hygrothermal behavior of solid brick walls", *Journal of Building Engineering*, Vol. 7, pp.121-132.

de Wolf, D.A. (2001), "On the Laws-Parsons distribution of raindrop sizes", *Radio Science*, Vol. 36 No. 4, pp.639-642.

Diedrichs, B., Sima, M., Orellano, A. and Tengstrand, H. (2007), "Crosswind stability of a high-speed train on a high embankment", *Proceedings of the Institution of Mechanical Engineers, Part F: Journal of Rail and Rapid Transit*, Vol. 221 No. 2, pp.205-225.

EN14067-6, 2010. Railway applications Aerodynamics-Part 6: Requirements and test procedures for cross wind assessment.

Giappino, S., Rocchi, D., Schito, P. and Tomasini, G. (2016), "Cross wind and rollover risk on lightweight railway vehicles", *Journal of Wind Engineering and Industrial Aerodynamics*, Vol. 153, pp.106-112.

Huang, S., Hemida, H. and Yang, M. (2016), "Numerical calculation of the slipstream generated by a CRH2 high-speed train", *Proceedings of the Institution of Mechanical Engineers, Part F: Journal of Rail and Rapid Transit*, Vol. 230 No. 1, pp.103-116.

Huang, S. and Li, Q. (2010), "Numerical simulations of wind-driven rain on building envelopes based on Eulerian multiphase model", *Journal of Wind Engineering and Industrial Aerodynamics*, Vol. 98 No. 12, pp.843-857.

Ikemori, M. (1978), "A Study of Track Maintenance for the Derailment due to the Interaction between Track and Vehicles", *Railway Technical Research Institute, Quarterly Reports*, Vol. 19 No. 1.

Jiang, S., Zou, Y., He, X., Cai, C., Zhai, L. and Nong, X. (2022), "Wind Tunnel Study on Aerodynamic Characteristics of the Train on Viaducts with a New Type of Wind-Noise Barrier Under Cross Wind", *International Journal of Structural Stability and Dynamics*, Vol. 22 No. 10, pp.2241004.

Jin, T., Liu, Z., Sun, S., Ren, Z., Deng, L., Ning, D., Du, H. and Li, W. (2020), "Theoretical and experimental investigation of a stiffness-controllable suspension for railway vehicles to avoid resonance", *International Journal of*

*Mechanical Sciences*, Vol. 187, pp.105901.

Kubilay, A., Derome, D., Blocken, B. and Carmeliet, J. (2013), "CFD simulation and validation of wind-driven rain on a building facade with an Eulerian multiphase model", *Building and environment*, Vol. 61, pp.69-81.

Kummitha, O.R., Kumar, R.V. and Krishna, V.M. (2021), "CFD analysis for airflow distribution of a conventional building plan for different wind directions", *Journal of Computational Design and Engineering*, Vol. 8 No. 2, pp.559-569.

Lai, Y., Zhang, M., Liu, Z. and Yu, W. (2006), "Numerical analysis for cooling effect of open boundary ripped-rock embankment on Qinghai-Tibetan railway", *Science in China Series D*, Vol. 49 No. 7, pp.764-772.

Li, H., Yu, M., Qian, Z. and Heng, W. (2020), "Numerical Simulation of Aerodynamic Characteristics of a High-speed Train Under Crosswind and Rain Conditions", *Fluid Dynamics & Materials Processing*, Vol. 16 No. 1, pp.77-90.

Li, T., Zhang, J. and Zhang, W. (2013), "A numerical approach to the interaction between airflow and a high-speed train subjected to crosswind", *Journal of Zhejiang University-SCIENCE A*, Vol. 14 No. 7, pp.482-493.

Li, W., Liu, T., Martinez-Vazquez, P., Guo, Z., Huo, X., Xia, Y. and Chen, Z. (2022a), "Effects of embankment layouts on train aerodynamics in a wind tunnel configuration", *Journal of Wind Engineering and Industrial Aerodynamics*, Vol. 220, pp.104830.

Li, X., Deng, J., Chen, D., Xie, F. and Zheng, Y. (2011a), "Unsteady simulation for a high-speed train entering a tunnel", *Journal of Zhejiang University-SCIENCE A*, Vol. 12 No. 12, pp.957-963.

Li, Y., Tian, H. and Yang, M. (2011b), "Aerodynamic drag analysis of double-deck container vehicles with different structures", *Journal of Central South University of Technology*, Vol. 18 No. 4, pp.1311-1315.

Li, Y., Xiang, H., Wang, Z. and Zhu, J. (2022b), "A comprehensive review on coupling vibrations of train-bridge systems under external excitations", *Railway Engineering Science*, Vol. 30 No. 3, pp.383-401.

Liu, M., Ma, W., Niu, F., Luo, J. and Yin, G. (2018), "Thermal performance of a novel crushed-rock embankment structure for expressway in permafrost regions", *International Journal of Heat and Mass Transfer*, Vol. 127, pp.1178-1188.

Liu, T., Wang, L., Chen, Z., Gao, H., Li, W., Guo, Z., Xia, Y., Huo, X. and Wang, Y. (2022), "Study on the pressure pipe length in train aerodynamic tests and its applications in crosswinds", *Journal of Wind Engineering and Industrial Aerodynamics*, Vol. 220, pp.104880.

Liu, T. and Zhang, J. (2013), "Effect of landform on aerodynamic performance of high-speed trains in cutting under cross wind", *Journal of Central South University*, Vol. 20 No. 3, pp.830-836.

Lu, C., Li, Q., Huang, S., Chen, F. and Fu, X. (2012), "Large eddy simulation of wind effects on a long-span complex roof structure", *Journal of Wind Engineering and Industrial Aerodynamics*, Vol. 100 No. 1, pp.1-18.

Mao, J., Ma, X. and Xi, Y. (2011), "Research on the running stability of high-speed trains under the cross wind by means of simulation", *Journal of Beijing Jiaotong University*, Vol. 35 No. 1, pp.44-48.

Montenegro, P., Barbosa, D., Carvalho, H. and Calçada, R. (2020), "Dynamic effects on a train-bridge system caused by stochastically generated turbulent wind fields", *Engineering Structures*, Vol. 211, pp.110430.

Niu, J., Zhang, Y., Li, R., Chen, Z., Yao, H. and Wang, Y. (2022), "Aerodynamic simulation of effects of one-and two-side windbreak walls on a moving train running on a double track railway line subjected to strong crosswind", *Journal of Wind Engineering and Industrial Aerodynamics*, Vol. 221, pp.104912.

Olmos, J.M. and Astiz, M.Á. (2018), "Non-linear vehicle-bridge-wind interaction model for running safety assessment of high-speed trains over a high-pier viaduct", *Journal of Sound and Vibration*, Vol. 419, pp.63-89.

Pettersson, K., Krajnovic, S., Kalagasidis, A. and Johansson, P. (2016), "Simulating wind-driven rain on building facades using Eulerian multiphase with rain phase turbulence model", *Building and Environment*, Vol. 106, pp.1-9.

Pietrzak, O. and Pietrzak, K. (2021), "Cargo tram in freight handling in urban areas in Poland", *Sustainable Cities and Society*, Vol. 70, pp.102902.

Rane, S. and He, L. (2020), "CFD analysis of flashing flow in two-phase geothermal turbine design", *Journal of Computational Design and Engineering*, Vol. 7 No. 2, pp.238-250.

Shao, X., Wan, J., Chen, D. and Xiong, H. (2011), "Aerodynamic modeling and stability analysis of a high-speed train under strong rain and crosswind conditions", *Journal of Zhejiang University-SCIENCE A*, Vol. 12 No. 12, pp.964-970.

Stark, P. and Fritsching, U. (2015), "Simulation of the impinging liquid jet cooling process of a flat plate", *International Journal of Numerical Methods for Heat & Fluid Flow*.

Tao, W., Lou, P., Zou, Y., Cai, C., He, X. and Jiang, S. (2022), "Effects of Curved Wind Barrier on the Aerodynamic Characteristics of a Train–Bridge System and Its Static Wind Load", *International Journal of Structural Stability and Dynamics*, Vol. 22 No. 10, pp.2241006.

TB10623-2014, 2014. Code for Design of Intercity Railway.

Wang, H., Song, W. and Chen, Y. (2019), "Numerical simulation of wind-driven rain distribution on building facades under combination layout", *Journal of Wind Engineering and Industrial Aerodynamics*, Vol. 188, pp.375-383.

Wen, J., Li, Q., Zhao, L., Huang, Q. and Lu, Z. (2022), "Aerodynamic Characteristics of Express Freight Train on Bridges Based on Wind Tunnel Tests", *International Journal of Structural Stability and Dynamics*, Vol. 22 No. 10, pp.2241005.

Xi, Y., Mao, J., Yang, G. and Fang, Y., (2012), "Research on influence of the type of cross wind field on the aerodynamic performance of a high-speed train", *Proceedings of the 1st International Workshop on High-Speed and Intercity Railways*, Shenzhen and Hong Kong SAR, China, Springer, pp.305-317.

Xie, G., Li, S., Sunden, B. and Zhang, W. (2014), "Computational fluid dynamics for thermal performance of a water-cooled minichannel heat sink with different chip arrangements", *International Journal of Numerical Methods for Heat & Fluid Flow*.

Xu, R., Qian, B., Wu, F., Li, X., Zhang, G. and Wang, L. (2022), "Dispersion of evaporating droplets in the passenger compartment of high-speed train", *Journal of Building Engineering*, Vol. 48, pp.104001.

Yang, W., Liu, Y., Deng, E., Wang, Y., He, X., Lei, M. and Zou, Y. (2022), "Field test and numerical reconstitution of natural winds at the tunnel entrance section of high-speed railway", *International Journal of Numerical Methods for Heat & Fluid Flow*, No. ahead-of-print.

Yang, Y., Zhang, B., Wang, T., Xu, H. and Wu, Y. (2019), "Two-axle test vehicle for bridges: Theory and applications", *International Journal of Mechanical Sciences*, Vol. 152, pp.51-62.

Yu, M., Liu, J. and Dai, Z. (2021), "Aerodynamic characteristics of a high-speed train exposed to heavy rain environment based on non-spherical raindrop", *Journal of Wind Engineering and Industrial Aerodynamics*, Vol. 211, pp.104532.

Yu, M., Liu, J., Zhang, Q. and Dai, Z. (2022), "Unsteady aerodynamic characteristics on trains exposed to strong wind and rain environment", *Journal of Wind Engineering and Industrial Aerodynamics*, Vol. 226, pp.105032.

Yu, X., Lang, M., Gao, Y., Wang, K., Su, C.-H., Tsai, S.-B., Huo, M., Yu, X. and Li, S. (2018), "An empirical study on the design of China high-speed rail express train operation plan—From a sustainable transport perspective", *Sustainability*, Vol. 10 No. 7, pp.2478.

- Zeng, C., Song, Y., Cai, D., Hu, P., Cui, H., Yang, J. and Zhang, H. (2019), "Exploration on the spatial spillover effect of infrastructure network on urbanization: A case study in Wuhan urban agglomeration", *Sustainable Cities and Society*, Vol. 47, pp.101476.
- Zhang, J., Gao, G., Liu, T. and Li, Z. (2017), "Shape Optimization of a Kind of Earth Embankment Type Windbreak Wall along the Lanzhou-Xinjiang Railway", *Journal of Applied Fluid Mechanics*, Vol. 10 No. 4, pp.1189-1200.
- Zhang, L., Yang, M. and Liang, X. (2018), "Experimental study on the effect of wind angles on pressure distribution of train streamlined zone and train aerodynamic forces", *Journal of Wind Engineering and Industrial Aerodynamics*, Vol. 174, pp.330-343.
- Zhang, M., Lai, Y., Gao, Z. and Yu, W. (2006), "Influence of boundary conditions on the cooling effect of crushed-rock embankment in permafrost regions of Qinghai-Tibetan Plateau", *Cold Regions Science and Technology*, Vol. 44 No. 3, pp.225-239.
- Zhang, P., Zhao, Y., Zhu, X., Cai, Z., Xu, J. and Shi, S. (2020), "Spatial structure of urban agglomeration under the impact of high-speed railway construction: Based on the social network analysis", *Sustainable Cities and Society*, Vol. 62, pp.102404.
- Zhang, T., Xia, H. and Guo, W. (2013), "Analysis on running safety of train on bridge with wind barriers subjected to cross wind", *Wind Struct*, Vol. 17 No. 2, pp.203-225.
- Zhao, H. and Zhai, W. (2015), "Effect of noise barrier on aerodynamic performance of high-speed train in crosswind", *Wind and Structures*, Vol. 20 No. 4, pp.509-525.
- Zhou, P., Li, T., Zhao, C. and Zhang, J. (2020), "Numerical study on the flow field characteristics of the new high-speed maglev train in open air", *Journal of Zhejiang University-SCIENCE A*, Vol. 21 No. 5, pp.366-381.
- Zou, Y., Liu, Z., Shi, K., Song, J., He, X. and Liu, Q. (2022), "Experimental Study of the Aerodynamic Characteristics of a Suspended Monorail Vehicle-Bridge System Under Crosswinds", *International Journal of Structural Stability and Dynamics*, Vol. 22 No. 10, pp.2241007.